Journal Name

ARTICLE TYPE

Cite this: DOI: 00.0000/xxxxxxxxxx

Multi-channel photodissociation and XUV-induced charge transfer dynamics in strong-field-ionized methyl iodide studied with time-resolved recoil-frame covariance imaging†

Felix Allum,[a] Nils Anders,[b] Mark Brouard,[a] Philip Bucksbaum,[c] Michael Burt,[a] Briony Downes-Ward,[d] Sven Grundmann,[b] James Harries,[e] Yudai Ishimura,[f] Hiroshi Iwayama,[g] Leon Kaiser,[b] Edwin Kukk,[h] Jason Lee,[i] Xiaojing Liu,[j] Russell S. Minns,[d] Kiyonobu Nagaya,[k] Akinobu Niozu,[k] Johannes Niskanen,[h] Jordan O'Neal,[c] Shigeki Owada,[l] James Pickering,[a] Daniel Rolles,[m] Artem Rudenko,[m] Shu Saito,[f] Kiyoshi Ueda,[f] Claire Vallance,[a] Nicholas Werby,[c] Joanne Woodhouse,[d] Daehyun You,[f] Farzaneh Ziaee,[m] Taran Driver,[c] and Ruaridh Forbes[c]

Received Date
Accepted Date

DOI: 00.0000/xxxxxxxxxx

The photodissociation dynamics of strong-field ionized methyl iodide (CH_3I) were probed using intense extreme ultraviolet (XUV) radiation produced by the SPring-8 Angstrom Compact free electron LAser (SACLA). Strong-field ionization and subsequent fragmentation of CH_3I was initiated by an intense femtosecond infrared (IR) pulse. The ensuing fragmentation and charge-transfer processes following multiple ionization by the XUV pulse at a range of pump-probe delays were followed in a multi-mass ion velocity-map imaging (VMI) experiment. Simultaneous imaging of a wide range of resultant ions allowed for additional insight into the complex dynamics by elucidating correlations between the momenta of different fragment ions using time-resolved recoil-frame covariance imaging analysis. The comprehensive picture of the photodynamics that can be extracted provides promising evidence that the techniques described here could be applied to study ultrafast photochemistry in a range of molecular systems at high count rates using state-of-the-art advanced light sources.

[a] *Chemistry Research Laboratory, Department of Chemistry, University of Oxford, Oxford OX1 3TA, United Kingdom*
[b] *Institut für Kernphysik, Goethe-Universität, Max-von-Laue-Strasse 1, 60438 Frankfurt am Main, Germany*
[c] *Stanford PULSE Institute, SLAC National Accelerator Laboratory, 2575 Sand Hill Road, Menlo Park, CA 94025*
[d] *Chemistry, University of Southampton, Highfield, Southampton SO17 1BJ, UK*
[e] *QST, SPring-8, Kouto 1-1-1, Sayo, Hyogo, 679-5148, Japan*
[f] *Institute of Multidisciplinary Research for Advanced Materials, Tohoku University, Sendai, 980-8577, Japan*
[g] *UVSOR Synchrotron Facility, Institute for Molecular Science, Okazaki 444-8585, Japan*
[h] *Department of Physics and Astronomy, University of Turku, Turku, FI-20014, Finland*
[i] *Deutsches Elektronen-Synchrotron (DESY), Notkestraße 85, 22607 Hamburg, Germany*
[j] *School of physical science and technology, ShanghaiTech University, Shanghai, 201210, China*
[k] *Department of Physics, Kyoto University, Kyoto, 606-8502, Japan*
[l] *RIKEN SPring-8 Center, Sayo, Hyogo, 679-5148, Japan*
[m] *J. R. Macdonald Laboratory, Department of Physics, Kansas State University, Manhattan, KS, 66506, USA*

† Electronic Supplementary Information (ESI) available: [details of any supplementary information available should be included here]. See DOI: 00.0000/00000000.

1 Introduction

A critical component of many physical, chemical and biological reactions is photo-induced electron transfer[1–3]. This plays a central role in processes ranging from photosynthetic light harvesting[4,5] to X-ray emission from comets[6] and has applications in photocatalysis[7]. At the microscopic level, charge transfer dynamics are driven by the coupled motion of the electronic and nuclear degrees of freedom within the system, and are hence governed by non-adiabatic dynamics[2,3]. Early time-resolved studies investigating charge transfer and migration dynamics exploited selective valence photoionization or photoexcitation to induce electron motion, which are less site-specific probes, when using techniques such as mass spectrometry[8–10] and time-resolved fluorescence[11,12], to track the ensuing dynamics.

The advent of intense, short-pulse radiation sources in the eXtreme UltraViolet (XUV) and X-ray domains, including High Harmonic Generation (HHG)[13] or Free-Electron Lasers (FELs)[14–16], provides a promising route to study localized charge transfer dynamics. This is due to the large X-ray absorption cross sections found in heavy elements, which can result in localization of multiple charges on a specific atomic site within a molecule, through a series of inner-shell photoionization events followed by associated Auger decay. The ability to spatially localize charge through multiple core ionization has recently been exploited to study charge rearrangement dynamics in polyatomic molecules[17–20].

Early time-resolved experiments exploiting X-ray FELs to study distance-dependent charge transfer dynamics included an XUV pump-probe experiment on I_2 at the Free-electron LASer at Hamburg (FLASH)[21] and two-color X-ray experiment on XeF_2 at the Linac Coherent Light Source (LCLS)[22]. While such studies benefited from high temporal resolution, the population of many dissociative channels by the pump pulse was a clear drawback. The first study to exploit a combination of an X-ray FEL and optical laser pulse was conducted by Erk *et al.*, where an InfraRed (IR) pump pulse was used to dissociatively ionize CH_3I and the charge transfer dynamics initiated by subsequent inner-shell X-ray ionization were probed at different pump-probe delays and, thus, at different internuclear distances[23]. Follow-up studies on CH_3I, conducted at both the LCLS[24] and FLASH[25,26] at the I 3d and 4d edges, respectively, further simplified the pump process by utilizing single-photon ultraviolet excitation for the pump step to initiate neutral photodissociation of the carbon-iodine bond. However, even with the simplification of data interpretation afforded by single photon excitation, these experiments all suffered from relatively long ($\geq$120 fs) temporal instrument response functions due to dispersion from propagation of the UV pulse through transmissive optics.

In this manuscript, we present results from a femtosecond IR-pump XUV-probe experiment exploiting inner-shell ionization at the I 4d edge to trace charge transfer dynamics in CH_3I. Dissociation of CH_3I target molecules is induced by an 800 nm IR pump pulse. The ensuing dynamics are then followed as a function of pump-probe delay (and hence internuclear separation) with an intense XUV pulse from the SPring-8 Angstrom Compact free electron LAser (SACLA)[27]. The pump laser intensity, $\sim 4\times10^{14}$W/cm^2, was significantly higher than that employed previously at the LCLS, $\sim 8\times10^{13}$W/cm^2 [23]. This produced two-body fragmentation into neutral and singly charged CH_3 and I fragments as well as some population of tricationic states, which resulted in doubly charged atomic iodine.

In spite of the close connection with the earlier work of Erk *et al.*, the present study has several important differences. First, the overall temporal resolution is significantly better, 68$\pm$14 fs Full Width at Half Maximum (FWHM), compared to 110$\pm$9 fs, FWHM[23]. This gives access to early time ($<$100 fs) photofragmentation dynamics and hence charge transfer signatures before the molecule has completely dissociated. Second, by exploiting XUV radiation at SACLA, we probe the I 4d (N-) edge[28] rather than the I 3d (M-) edge, which was the subject of the earlier LCLS investigations[23,24]. Recent publications using synchrotron radiation[29–31] show that the available Auger decay pathways are substantially different following 3d and 4d ionization. For the I N-edge, the molecular Auger decay (NVV) involves exclusively valence electrons[31], involved in molecular bonding, whereas the M-edge is dominated by $MN_{4,5}N_{4,5}$ transitions at the I atomic site[29,30]. This difference also has important consequences for the number of charges localized on the I atom per XUV or X-ray photoabsorption event. For the closely related system of Xe, two to three charges are typically found for photoionization and Auger decay at a photon energy of 100 eV, which increases to between four and six charges at a photon energy of 750 eV[32]. It is therefore prudent to understand the role of the probing mechanism at a specific atomic edge. Finally by utilizing a Velocity-Map Imaging (VMI) spectrometer coupled with the Pixel Imaging Mass Spectrometry (PImMS) camera[33,34], we are able to simultaneously record a wide range of ionic fragment momenta on a shot-by-shot basis at high count rates ($\sim$80 ions shot^{-1}). This capability permits us to extract correlations between different ionic fragments using covariance analysis[35]. In particular, by utilizing time-resolved recoil-frame covariance imaging[36–39], the role of multiple dissociative ionization and Coulomb explosion channels induced by the IR pump pulse, as well as different probe ionization pathways, can be disentangled.

This article is structured as follows. In Section 2, the experimental setup is described in detail. Section 3 outlines the data analysis method used to process IR-FEL data, with a focus on recoil-frame covariance imaging in Section 3.1. The experimental results and associated discussion are contained in Section 4, which is subdivided into: dynamics induced by the pump pulse (Section 4.1); the IR-XUV dynamics (Section 4.2); and information content offered by performing covariance imaging (Section 4.3). Finally, our conclusions are summarized in Section 5.

2 Experimental Methods

The experiment was conducted at the soft X-ray beamline (BL1) of SACLA[27], which delivers ultrashort XUV FEL pulses in the $h\nu = \sim$40-150 eV range at a repetition rate of 60 Hz. For the experiments presented here, a photon energy of 95 eV was selected to coincide with

the maximum of the I $4d_{5/2,3/2} \rightarrow \varepsilon f$ shape resonances[28,31]. A photon bandwidth of approximately 2% ($\Delta E/E$) and a pulse duration of 30 fs were utilized[40]. A Kirkpatrick–Baez (KB) mirror system focused the FEL pulse to a spot size of $\sim 10 \mu$m ($1/e^2$) at the interaction point of an experimental chamber. An upstream gas intensity monitor permitted single shot FEL pulse energy measurements to be recorded, typical values ranged from 5-25 μJ in this experiment. The energy on target is expected to be approximately 90% of that measured at the gas intensity monitor[27]. For the employed pulse energies and focal spot size diameter, based on Gaussian beam optics, an upper limit of $\sim 2 \times^{15}$ W/cm^2 was obtained for the XUV intensity.

The pump-probe laser system comprised a Ti:sapphire oscillator (Coherent Inc., Vitara), a chirped-pulse regenerative amplification system (Coherent Inc., Legend Elite), and a home-built multipass amplifier[27] operating at 60 Hz. This system is capable of producing 10 mJ, 40 fs pulses at a central wavelength of 800 nm after compression at the experimental end station. Pulses at the laser fundamental wavelength served as the strong-field ionization pump, and a maximum pulse energy of 1.8 mJ was utilized. A computer-controlled variable neutral density filter and optical delay stage provided control of laser attenuation and relative timing between laser and FEL pulses, respectively. The intense 800 nm pump pulses were focused to the centre of the experimental chamber using a lens (f = 2 m) mounted adjacent to the window for laser incoupling. Based on focal geometry, pulse energies, as well as duration, a peak intensity of $4\times \sim 5 \times^{14}$ W/cm^2 and spot size of $\sim 42 \mu$m ($1/e^2$) are determined for the IR pump pulse, respectively. A right angle prism mirror was used to recombine the laser and FEL beams in a nearly collinear geometry ($<0.5^\circ$ crossing angle).

The employed apparatus consisted of a differentially-pumped molecular beam source and a main (interaction) chamber[41]. Commercially available, room temperature CH_3I (>99.5% Tokyo Chemical Industry Co.) was expanded, after multiple freeze-thaw-pump cycles, into the interaction chamber via a skimmer using a pulsed jet (General Valve) without carrier gas. The molecular beam intersected the laser/FEL axis at angle of $\sim 45^\circ$. Ions generated from the interaction between the molecular, infrared and XUV beams were accelerated by electrodes optimized for velocity-mapping[42] and projected onto a 75 mm diameter dual MicroChannel Plate (MCP) detector backed by a phosphor screen (P46). The polarization vectors of both laser beams were parallel to the MCP detector surface. Emission from the phosphor screen was imaged by the PImMS camera[33,34]. The camera was equipped with a PImMS2 sensor, which is comprised of a 324×324 pixel detector that recorded the spatial positions (x, y) and arrival times (t) of the light from the phosphor with a precision of 25 ns. Time-stamping of up to two ion hits per pixel per shot permitted the camera to operate at 30 Hz (i.e. half the SACLA repetition rate). This multiplexed spatial and temporal information means that all ionic fragments within a single laser shot can be recorded, permitting correlations to be extracted in different channels via covariance analysis (imaging)[36,39].

Photoion images were recorded as a function of laser-FEL time delay from approximately -0.5 to 2.5 ps in variable step sizes. The temporal overlap and instrument response function of the laser and FEL pulses were characterized *in situ* using the ratio of Xe^{2+}/Xe^{3+} in a two-color (IR+FEL) experiment. This ratio is reduced when the FEL precedes the IR pulse, due to the IR pulse post-ionizing metastable Xe^{2+} ions formed after Xe (4d) photoionization and subsequent Auger decay[43–45]. Fitting this ratio as a function of time delay to a normal Cumulative Distribution Function (CDF) yielded an instrument response function of 68±14 fs, placing an upper limit on experimental time-resolution. This procedure also yielded the calibrated time-zero for the pump-probe experiments, via the center of the CDF. Fluctuations in the laser-FEL timing were monitored on a shot-to-shot basis using the transient reflectivity change in a GaAs wafer[46].

3 Data Processing and Analysis

Individual ion events recorded by the time-stamping camera generally span multiple pixels and time bin registers. Consequently, the recorded data were centroided in both time and in position, as described previously[36], for all presented data apart from the covariance analysis. For the time-resolved data presented in Sections 4.2 and 4.3, data acquired over several scans of the IR laser delay were summed, following correction for the FEL timing jitter[46]. Data was then sorted by pump-probe delay into 25 fs bins, and the total signal per pump-probe delay bin was normalized by the average FEL pulse energy for the summed shots. Three-dimensional velocity distributions for individual ions were reconstructed from the recorded two-dimensional projections using the pBASEX algorithm[47]. Prior to this, images were symmetrized, excluding quadrant(s) which were compromised by a region of very low sensitivity near the centre of the detector. Calibration of radius of the ion images to kinetic energy was performed using literature values for the KER of the two channels observed in the IR-induced (1,1) Coulomb explosion of CH_3I[48].

3.1 Recoil-frame covariance imaging

By simultaneously recording images for all ionic fragments within each experimental cycle, correlations between the momenta of different fragments can be determined. At sufficiently low count rates (<1 ions shot^{-1}), ions detected in a single acquisition cycle (i.e. each laser shot) can be assumed to come from the same target molecule. At the relatively high count rates employed in the current experiments ($\sim$ 10s ions shot^{-1}), this assumption no longer holds. However, correlated information can still be extracted through covariance analysis[35,49]. Initially this was applied to determine correlations between different dissociative ionization channels in the Coulomb explosion dynamics of small molecules, but the approach has subsequently been extensively developed for other applications[49], particularly in FEL science[50–53]. Briefly, covariance is a measure of the linear correlation of two variables, X and Y, defined as:

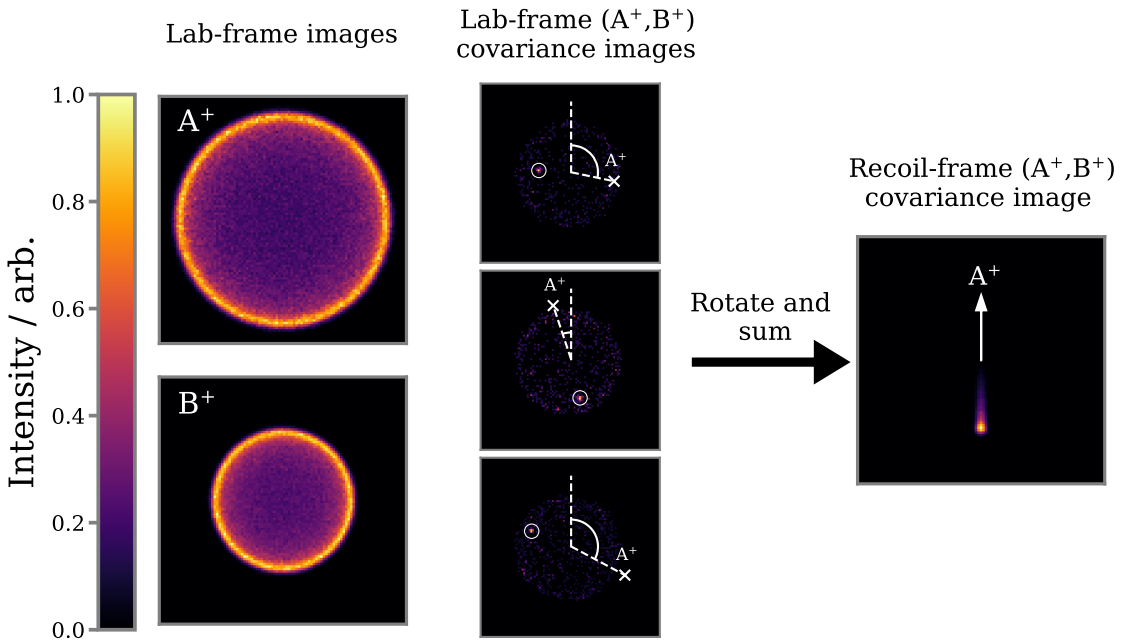

Fig. 1 Schematic of the recoil-frame covariance imaging technique between two ions: A^+ and B^+ (first column). For each pixel in the image of the A^+, 'reference' ion, covariance with each pixel in the B^+ image is calculated. Example covariances for different pixels in the A^+ image are shown in the second column, showing intensity in the regions circled. These images are rotated by the marked angle and summed to give the recoil-frame covariance image, shown in the final column.

$$\text{Covariance}(X,Y) = \langle XY \rangle - \langle X \rangle \langle Y \rangle \tag{1}$$

In the current experiment, two-dimensional velocity information is recorded on a shot-to-shot basis for each ion. Calculating the two-fold covariance between each pixel of the ion images for a pair of fragments therefore yields a four-dimensional covariance array. An intuitive way to reduce this to an informative two-dimensional representation is to transform the covariance into the recoil frame of one ion, denoted the 'reference' ion. This process is illustrated for simulated data for the Coulomb explosion of a diatomic molecule, AB, into A^+ and B^+ ions in Figure 1. For these simulations, only this dissociation channel was accounted for. 100,000 laser shots were simulated, with a mean event rate of 25 frame^{-1} (following Poisson statistics) and a detection efficiency of 50%.

For a specific pixel in the reference ion (A^+) image, the covariance with the entire B^+ image is calculated. The resultant laboratory-frame covariance image can be interpreted as the recorded velocity distribution of the B^+ ion, given an A^+ ion is detected at the specified pixel. Illustrative images for three pixels of the reference A^+ ion image are plotted in the second column of Figure 1. In each case, signal at an angle of 180 degrees to the reference pixel can be observed, which is expected due to momentum conservation in the simulated two-body system. Each individual lab-frame covariance image is rather noisy, however, even in this idealised case, due to relatively small signal recorded in a given individual reference pixel. By rotating each calculated lab-frame covariance image by the angle between the reference pixel and an arbitrary vector (here chosen to be along the vertical) and summing, a recoil-frame covariance image is obtained. This is shown in the final column of Figure 1. This represents the velocity distribution of B^+ formed in conjunction with A^+ ions recoiling along the vertical direction. It should be noted that in the present work, only velocity information in the plane of the detector is recorded. As such, the transformation into the recoil frame can only be made in the detector plane. This restriction can be circumvented in a three-dimensional velocity-map imaging experiment[54]. In the case of two ions recoiling at approximately 180 degrees from one another, the 'true' covariance signal is focused to a relatively small region of the covariance map, as a result of this transformation into the recoil frame. This is a crucial benefit in experiments at access time-restricted facilities such as FELs, allowing for adequate signal-to-noise in the resulting covariance images from relatively short acquisition times. In the present work, this is found to hold even under the unstable experimental conditions typically observed at FELs.

Recoil-frame covariance imaging with a timestamping sensor has previously been applied to study the Coulomb explosion dynamics of complex molecules[36,38] and distinguish structural isomers[55] and enantiomers[56]. Incorporation of recoil-frame covariance analysis into tabletop femtosecond pump-probe Coulomb explosion imaging experiments has been used to study the neutral photodissociations[39] and coherent vibrational dynamics[37]. As explored in Section 4.3, recoil-frame covariance imaging can be applied in the present work to extract velocity distributions for individual breakup channels following strong-field ionization and (multiple) further ionizations by the XUV FEL pulse.

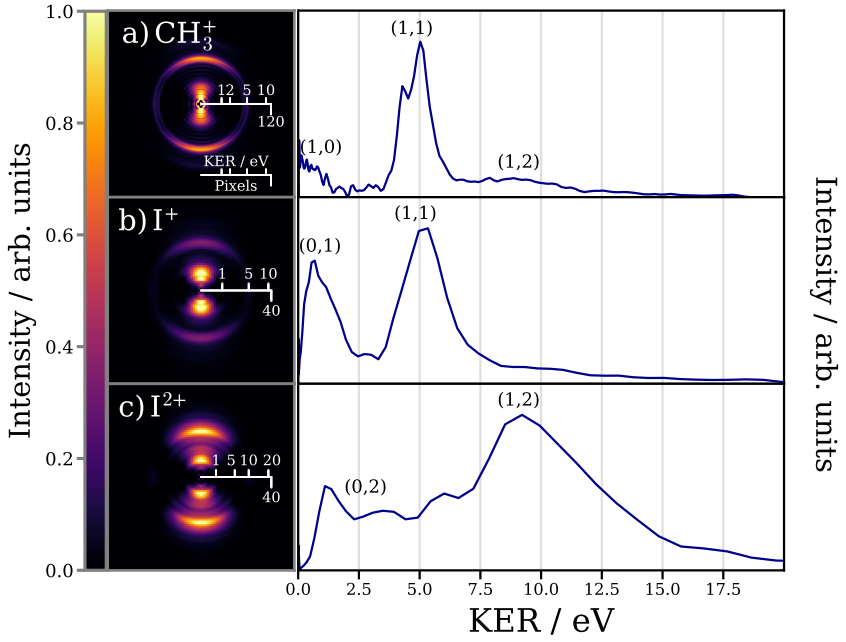

Fig. 2 IR-only velocity-map ion images (left) and KER distributions (right) for the (a) CH_3^+, (b) I^+ and (c) I^{2+} ions. Assigned channels are labelled (p, q) for dissociations to $CH_3^{p+}+I^{q+}$. The polarization axis of the IR laser is vertical and in the plane of the detector. The ion images have been Abel inverted using the pBASEX algorithm[47].

4 Results and Discussion

4.1 Strong-field ionization and fragmentation of CH_3I

The ionization and dissociation dynamics of CH_3I following exposure to intense IR light has been the subject of several previous studies[48,57–63]. The ionic states populated and the resultant kinetic energy and angular distributions of the fragment ions are sensitive to both the duration and intensity of the IR pulse. Therefore, in order to fully interpret the pump-probe results of the current work, it is first necessary to consider the effects of the IR field alone. At the intensities employed in the current work, multiple ionic dissociation pathways are observed, primarily originating from the CH_3I cation, dication and trication.

Figure 2 shows the Abel-inverted[47] VMI images and associated kinetic energy release (KER) distributions for the main photofragments (CH_3^+, I^+, I^{2+}) produced following IR ionization. For each ion, the total KER has been calculated assuming a two-body dissociation of CH_3I. Distinct features at different radii in these images are observed, resulting in peaks in the associated KER spectrum. Assigned breakup channels to produce $CH_3^{p+}+I^{q+}$ are labelled (p, q). In all cases, fragment ions are predominantly produced along the polarization axis of the IR laser (vertical). Dissociation of CH_3I^+ gives rise to low kinetic energy CH_3^+ or I^+ ions, whilst fragmentations of multiply charged parent molecules to yield multiple charged ions are at significantly higher KER, as expected due to Coulombic repulsion. As observed previously[39,48,63,64], these Coulomb explosion channels have a lower KER than that predicted by Coulomb's law for the equilibrium structure CH_3I (6.73 eV and 13.46 eV for the (1,1) and (1,2) channels, respectively). This deviation from Coulombic behaviour is supported by wavepacket simulations on *ab initio* potential energy curves performed by Corrales *et al.*[48,64]. In the case of the (1,1) channel, the KER distribution exhibits two bands (which can be resolved in panel a) of Figure 2), arising from dissociations on potential energy curves converging on different electronic states of the I^+ cation.

In the case of I^{2+}, ions with significantly lower velocity than those from the (1,2) channel ($\sim$9 eV) are produced and assigned to a charge-asymmetric (0,2) dissociation of CH_3I^{2+}. Such charge-asymmetric dissociation channels in intense laser fields have been the subject of several studies, particularly in homonuclear diatomic molecules such as O_2, N_2 and I_2[65–68], but are considered to be a more general strong-field phenomenon including for polyatomic molecules[69–71]. The channel labelled as (0,2) (see Figure 2(c)) is particularly broad, spanning a KER of $\sim$1-6 eV and there appears to be some structure within this feature (i.e. multiple bands). These could suggest different pathways are in operation, although in the current data, the resolution at low KER in the I^{2+} image is relatively poor. This is because operating the spectrometer at high enough extraction voltages to focus high-velocity CH_3^+ ions onto the detector necessarily results in a small I^{2+} image, due to the large disparity in the masses of the iodine and methyl fragments leading to far greater dissociation velocities for the CH_3^+ fragment. Additional data recorded at lower extraction voltages (shown in ESI Figure S4) to expand the I^{2+} image similarly exhibit some structure in the (0,2) feature, showing distinct broad peaks centered at approximately 1.5 and 4 eV.

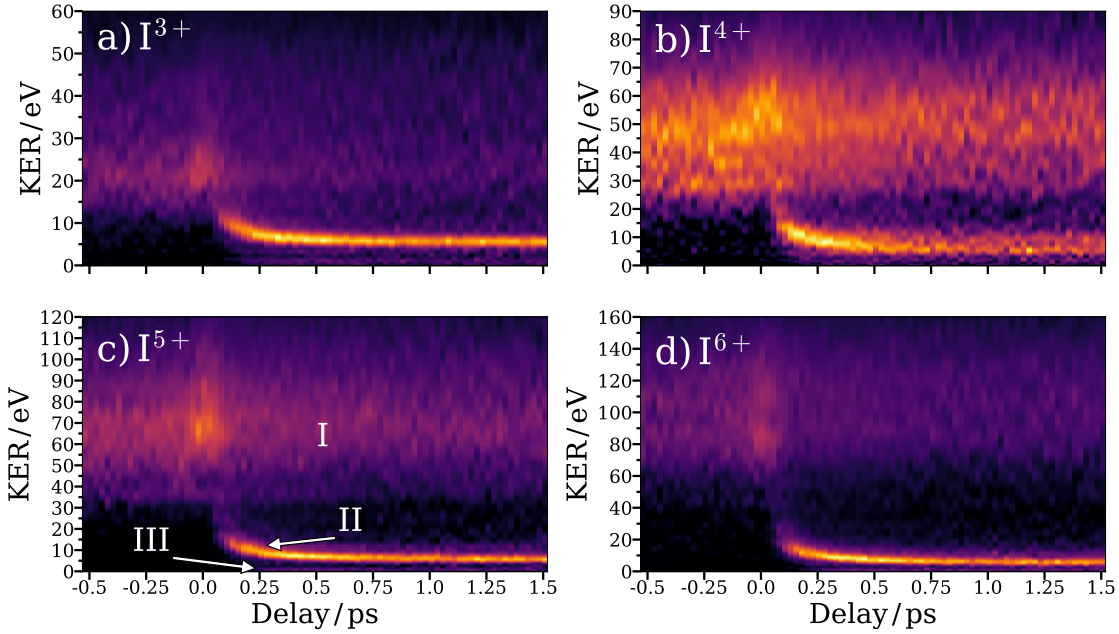

Fig. 3 Delay-dependent KER distributions for the a) I^{3+}, b) I^{4+}, c) I^{5+} and d) I^{6+} ions. These are obtained through angular integration of the appropriate time-resolved ion images, following Abel inversion using the pBASEX algorithm. The intensities for each ion are normalised separately, and plotted on the color scale shown in Figure 2. Negative delays correspond to the FEL probe pulse arriving before the IR pump pulse, and *vice versa*. For the I^{5+} ion, the main features observed are labelled, as discussed in the text.

4.2 IR-XUV Pump-probe

By following the intense IR pulse with an XUV pulse, products from the IR-induced ionic fragmentation of CH_3I can be further ionized by the XUV. At the employed XUV photon energy, the photoionization cross-section is dominated by ionization from the I 4d orbital, owing to $4d_{5/2,3/2} \rightarrow \varepsilon f$ shape resonances[28,31] in this energy region. Based on oscillator strengths extracted from dipole (e,e) spectroscopy, an approximately 15 times higher cross section is expected for the I 4d shell when compared to the total valence ionization contribution[28]. As such, post-ionization by the XUV pulse predominantly produces highly charged iodine atoms. In the case of the previously discussed (1,1) and (1,2) channels, further ionization at the iodine site by the XUV will lead to an increased Coulombic repulsion against the CH_3^+ produced by IR pulse. As this Coulombic repulsion is dependent on the internuclear separation of the two recoiling fragments, varying the pump-probe delay will lead to a delay-dependent KER of these highly charged iodines. Studying this channel as a function of pump-probe delay therefore tracks the internuclear separation of the dissociation products as a function of time[63,64,72–74].

Furthermore, creation of high iodine charge states by the XUV pulse can lead to charge-transfer to the associated methyl fragment. By varying the pump-probe delay, it is possible to infer dependence on delay (and therefore internuclear distance) of these charge-transfer processes. Charge-transfer is favored only for small internuclear separations, and is known to exhibit a dependence on the charge state of the two sites between which electron(s) are transferred, with higher charge states allowing for transfer over longer distances[23,75]. Performing this time-resolved experiment therefore allows for a great wealth of information about the femtosecond dynamics of both the strong-field fragmentation of CH_3I and the possible charge transfer pathways which are enabled by multiple XUV ionizations. In this section, these dynamics are studied through analysis of the delay-dependent ion yields and velocity-mapped images of the I^{n+} (n=1-10) fragments recorded. In Section 4.3, complementary information is given by delay-dependent velocity distributions for specific correlated pairs of I^{n+}, CH_x^{m+} fragments, which are extracted through recoil-frame covariance analysis[39].

Figure 3 shows the delay-dependent KER distributions for several I^{n+} ions (n=3-6). Broadly speaking, three main channels are observed for all the I^{n+} ($n > 2$) ions which can be detected and resolved in the experiment. These exhibit a similar form to features observed in previous studies[23–25] and can be attributed to a combination of ground-state Coulomb explosion as well as further ionization of the dissociative ionization channels induced by the IR pump pulse (see Section 4.1). Each of these channels will be discussed in turn and we adopt the same naming convention as previous studies[23,25]. Delay-dependent KER distributions for all I^{n+} (n=1-10) fragments are plotted in the ESI, as are delay-dependent velocity distributions, in which the lowest velocity features can be more clearly seen.

4.2.1 Channel I

A broad feature at high KER is observed (labelled I in Figure 3(c)), which, through comparison with the XUV only spectra (shown in ESI Figure S3), can be readily assigned to Coulomb explosion of CH_3I following multiple ionization of the neutral ground state. The transient yield of channel I displays two notable points: an enhancement of the total yield close to the time-zero and; a slight decrease in intensity after the temporal overlap. The latter point can be rationalized by depletion of the neutral ground state through strong-field

ionization by the IR pulse. Variation in the channel I yield is observed as a function of iodine charge state, with a noticeable decrease in the appearance at higher iodine charges relative to the other channels.

Despite the weak temporal dependence, analysis of the angular dependence of this channel reveals a more striking behavior. This is shown in ESI Figure S5, which displays VMI images for the the I^{5+} fragment ion at a series of pump-probe delays. Highlighted is a pronounced change in the angular anisotropy within the first picosecond for positive delays. Specifically, at negative delays (see Figure 7), channel I exhibits a largely isotropic distribution, with respect to the laser-FEL polarization direction (vertical), which becomes highly peaked along the polarization axis at approximately 300 fs and more isotropic towards longer delays. In a similar manner to Erk *et al.*[23], we attribute this feature to impulsive alignment of CH_3I, where the most polarizable molecular axis aligns with the direction of the electric field (the IR polarization axis)[76]. Detailed analysis and modeling of the alignment dynamics is considered beyond the scope of the present work and we merely remark on their presence in the recorded data.

4.2.2 Channel II

The most apparent time-dependent feature displays a decreasing KER as a function of pump-probe delay directly after time-zero, labelled Channel II in Figure 3. As observed previously[23–25,39,72,73], this decreasing KER is due to a Coulombic repulsion induced following ionization by the probe XUV pulse. This channel therefore involves a charged methyl cofragment. At shorter pump-probe delays, the Coulombic repulsion between the charged fragments is greater, leading to the observed dynamic kinetic energy distribution. For all iodine charge states, with the exception of I^{4+}, the kinetic energy release associated with Channel II at long pump-probe delays (shown for the I^{5+} ion in Figure 7) agrees well with that of the IR-only (1,1) channel. The discrepencacy observed for in the I^{4+} ion is discussed in detail in Section 4.2.4.

Further insight into the dynamics associated with Channel II can be gained through modelling and/or fitting the experimental data[39,73]. There are two contributions to the kinetic energy release of this channel at a given pump-probe delay: i) the kinetic energy gained *via* acceleration on the dicationic potential energy surface populated by the IR excitation and ii) the kinetic energy arising from repulsion between the two charged fragments following post-ionization by the XUV pulse. Under the assumptions of a single dissociation velocity, v_{rel}, which is instantaneously reached, and that the ions repel Coulombically following post-ionization by the XUV pulse, the kinetic energy release as a function of pump-probe delay, t, is given by[72]:

$$\mathrm{KER} = \mathrm{KER}_{(1,1)} + \frac{k_e q_{\mathrm{CH_3}} q_{\mathrm{I}}}{r_{\mathrm{eq}} + v_{\mathrm{rel}} t} \tag{2}$$

where $\mathrm{KER}_{(1,1)}$ is the KER of the IR-induced (1,1) channel, r_{eq} is the equilibrium C-I bond distance, and q_{CH_3} and q_I are the final charges on the CH_3 and I fragments, respectively.

Figure 4 overlays the delay-dependent KERs from this Equation 2 atop the experimental data for the I^{3+} and I^{6+} ions, assuming a

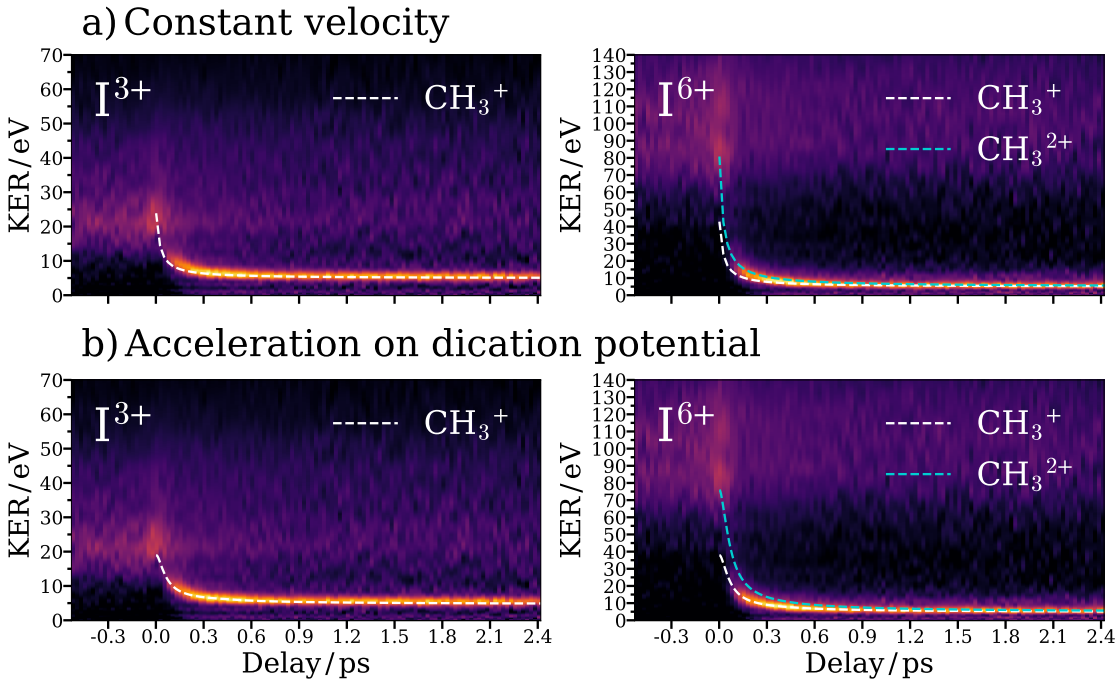

Fig. 4 Simulated delay-dependent KERs for channel II shown for the I^{3+} and I^{6+} ions. a) Simulations assuming constant recoil-velocity after time-zero is assumed b) Simulations incorporating acceleration on an example computed CH_3I^{2+} potential, as described in the text.

$KER_{(1,1)}$ of 5.20 eV (approximate peak KER for the (1,1) explosion, as shown in Figure 2). For the I^{6+} ion, calculated KERs for singly and doubly charged methyl fragments are included. For higher iodine charge states, Channel II appears to extend towards higher kinetic energy releases at short pump-probe delays than is predicted given a singly charged methyl fragment, which is indicative of a more highly charged cofragment. Multiply charged methyl fragments could feasibly be formed at short pump-probe delays either by charge-transfer from a highly charged iodine ion to the CH_3^+ ion, or through further ionization by an XUV photon at the methyl group (as is explored in more detail in Section 4.3). In general, the agreement between the simulated KER and the experimental KER for Channel II is good, although it can be seen that the agreement is relatively poor in the first few hundred fs following time-zero. The experimental KER of Channel II appears to decrease more gradually than the model predicts, leading to the model underestimating the KER in the ~100-300 fs region. This disagreement persists throughout the iodine charge states measured, and the discrepancy appears to increase for higher iodine charge states.

A likely cause for the inadequacy of the above simple model is the assumption that the fragments are instantaneously accelerated to their final velocities following double ionization by the IR pump pulse. In general, some finite time must be taken for the wavepacket to accelerate on the populated surfaces of the dication. Furthermore, as explored previously by Bañares and coworkers[48], several of the potential energy surfaces responsible for the IR-induced (1,1) Coulomb explosion of CH_3I are surprisingly shallow (deviating considerably from purely Coulombic potentials) near the C-I equilibrium bond length. This relatively shallow region of the potential energy surfaces will translate directly to a longer time taken for the fragments to accelerate to their asymptotic velocities.

In order to account for the effect of acceleration on the different dicationic potentials populated by the pump pulse, classical dynamics simulations on the computed potentials of Bañares and coworkers[48] were carried out. These were performed in timesteps of 0.1 fs using the Verlet method[77]. At each delay, the calculated velocity was converted to KER, and added to a Coulombic repulsion determined using Coulomb's law for the charge state of interest. Full simulated results for all the computed potential energy surfaces, including comparison to a purely Coulombic dication PES, are shown in the ESI Figures S6-S9. An example simulated result is shown in Figure 4b) for a state of CH_3I^{2+} correlated with $^3P_1$ I^+. Here, agreement with the experimental data is much stronger at short pump-probe delays. More accurately considering the acceleration during the (1,1) Coulomb explosion leads to shorter simulated internuclear distances as a function of pump-probe delay in comparison to the simple model assuming a constant recoil velocity. As a result, the Coulombic KER following XUV-ionization is greater in this model, and therefore the total KER is no longer underestimated in the first ~100-300 fs.

In summary, Channel II can be confidently assigned to (1,1) Coulomb explosion initiated by the IR pulse (with the exception of a contribution from the (1,2) channel in the I^{4+} ion, as discussed in Section 4.2.4), followed by further ionization predominantly at the iodine by the XUV pulse. Detailed modelling of this feature highlights the power of time-resolved Coulomb explosion imaging to study femtosecond wavepacket dynamics[39,63,64,72,73]. The precise delay-dependence of the measured KERs provide signatures of the evolution of the nuclear wavepacket on the potential energy surface(s) populated by the pump pulse. In particular, this signal appears

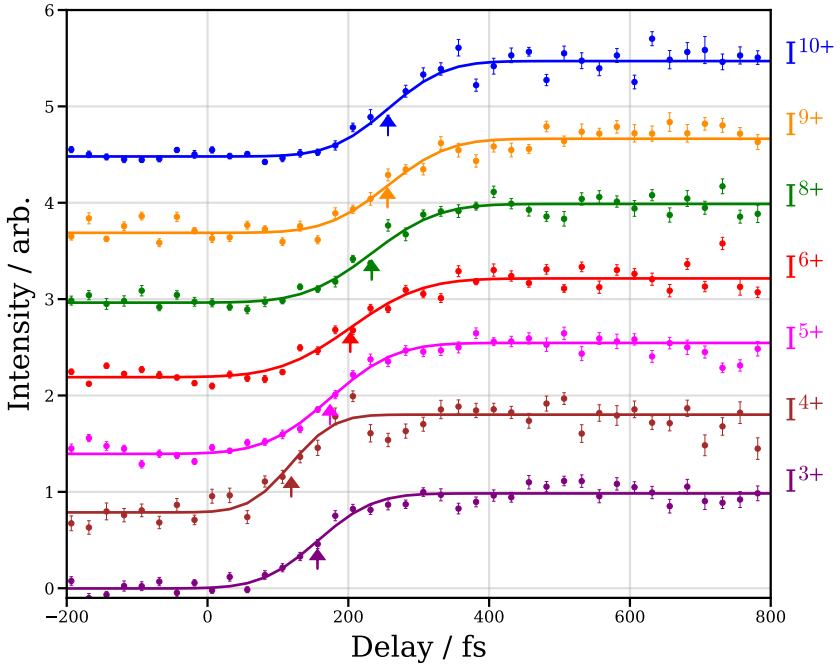

Fig. 5 Integrated ion yields as a function of pump-probe delay for Channel III for different iodine charge states, obtained by integrating the corresponding KER spectra below ~3.5 eV. The data are quoted with standard errors determined from a bootstrapping analysis of the dataset. The data have been fit to a Gaussian cumulative distribution function, as described in the text. The centres of the CDF fits are marked with coloured arrows.

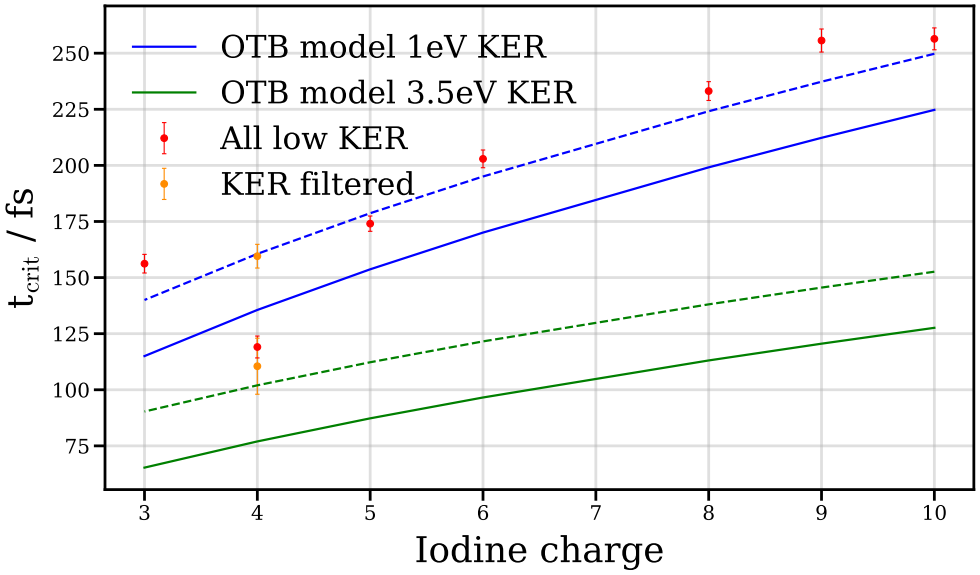

Fig. 6 Comparison between critical charge transfer time, t_{crit} extracted from the fitting of the low kinetic energy ion yields (red circles) and predicted by the over-the-barrier model for different kinetic energy release values (solid lines). These predictions, shifted 25 fs later to account for the acceleration of the fragments during the dissociation are plotted as dashed lines. For the I^{4+}, additional results for the two different kinetic energy ranges analysed in Figure 8 are included (gold circles).

to be sensitive to the precise shape of the potential energy surface in the region of the equilibrium bond distance. This is demonstrated through simulations incorporating previously calculated *ab initio* potentials[48].

4.2.3 Channel III

As discussed previously, and explored in several previous experiments[23–25,31], the intensity of the low KER feature (Channel III) as a function of pump-probe delay and iodine charge state provides a probe of the ensuing charge-transfer dynamics. This is because at suitably short pump-probe delays, XUV ionization at the iodine site, following (0,1) dissociation, will lead to charge transfer to the neutral methyl site. As such, this channel is only observed when charge-transfer does not occur, and so the intensity of this feature can be related to the probability of charge transfer between the recoiling highly charged iodine ion and the neutral methyl fragments at a given pump-probe delay, and therefore internuclear separation. Based on comparison between the asymptotic KER values for Channel III, for all investigated iodine charge states, and the IR-only results for I^+ (see Figure 2), it is apparent that this feature originates from a (0,1) fragmentation. Similarly to the discussion outline for Channel II, there exists variation between the low KER features observed for I^{4+} when compared to other charge states, which will subsequently be discussed in Section 4.2.4.

Shown in Figure 5 are yields for Channel III as a function of iodine charge state. A clear dependence on the transient onset time is observed, with lower charge states rising at earlier pump-probe delays when compared to the higher charge states. To quantify the variation in the onset times, we follow the fitting procedure outlined by Erk *et al.*[23], and utilize a Gaussian Cumulative Distribution Function (CDF), where the Gaussian width includes a contribution from the temporal instrument response function (see Section 2). Displayed as coloured arrows in Figure 5 are the onset times extracted from the fit of the Channel III feature for each iodine charge state.

By invoking a classical over-the-barrier (OTB) charge transfer model for a two-center system, the onset time can be related to the critical time, and therefore distance, at which charge transfer can no longer occur[23,75,78]. Physically, this can be viewed as the critical distance at which the height of the classical potential barrier separating the two centers (i.e. CH_3 and I fragments) becomes larger than the binding energy of the valence electrons. This results in localization of the electrons around one particular site and a halt to charge transfer. For the case of electron transfer from iodine with charge n to a neutral CH_3 considered here, the critical distance, r_{crit} is given in atomic units by:

$$r_{crit}(n) = \frac{1+2\sqrt{n}}{IP_{CH_3}} \tag{3}$$

where IP_{CH_3} is the ionization energy of the methyl radical.

Highlighted in Figure 6 is the comparison between the experimentally determined critical charge transfer times and those predicted from the OTB model, assuming a fixed KER and therefore a fixed recoil velocity of the fragments. These predictions are made assuming typical KERs for the (0,1) channel (blue) and the (0,2) channel (green). The predicted values from this model capture the trends observed in the data well, but in all cases the experimentally determined critical times are greater than those predicted. A similar

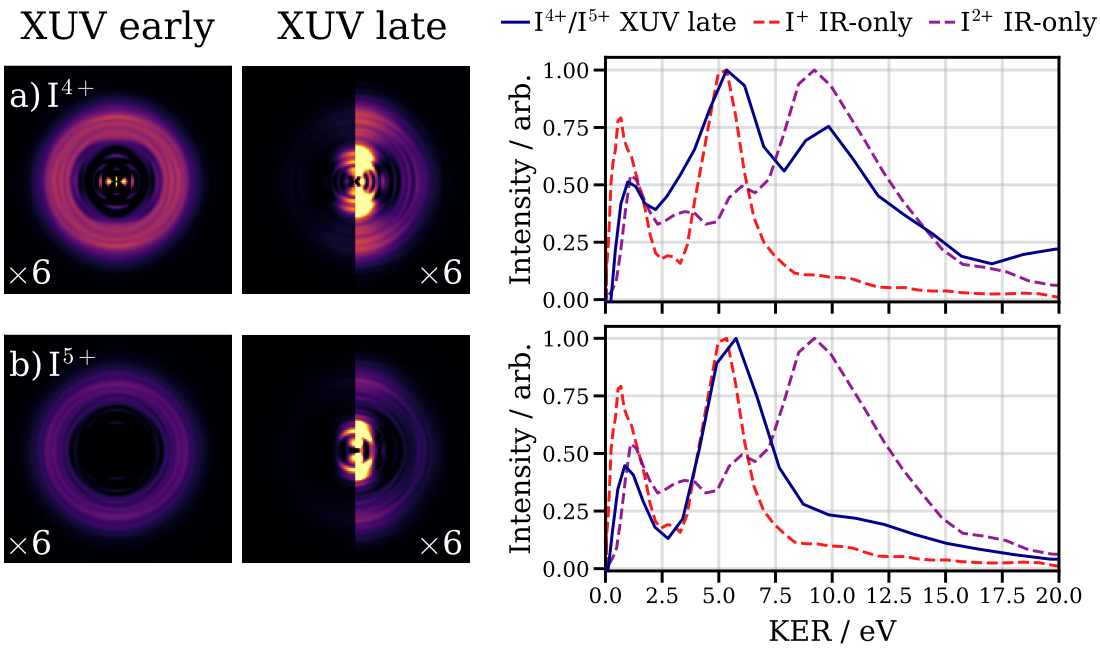

Fig. 7 Abel inverted velocity-map ion images (left) and KER distributions (right) for the (a) I^{4+} and (b) I^{5+} ions. XUV early and XUV late images are displayed, corresponding to negative and positive (>2 ps) pump-probe delays, respectively. To increase the visibility of weak features at high KER, the intensity of the XUV early image has been multiplied by 6, as has the right hand side of the XUV late image. The IR-only KER distributions of the I^+ (red) and I^{2+} (purple) ions are plotted for comparison.

rationale to that employed in Section 4.2.2 is valid here - the assumption that the fragments instantly reach their asymptotic velocity underestimates the time taken to reach the critical distance for charge transfer. This can be roughly accounted for by adding a delay offset to these predicted critical times, as shown by the dashed lines for a 25 fs offset. Good agreement is now observed across all considered charge states, once more indicating that within current experimental limitations, the OTB model seems to accurately encapsulate the measured charge- and distance- dependent of the probability of charge-transfer[23–25,31]. The present results additionally highlight that for increasingly accurate probing of these charge transfer processes, the exact dynamics of the dissociation channel(s) at play need to be well understood[79]. The I^{4+} ion appears to be an outlier, for which a deviation of approximately 50 fs from the predicted value is observed. We believe this is due to higher KER (0,2) channels contributing in the I^{4+} case. These different channels are discussed in Section 4.2.4.

4.2.4 Observation of (2,1) and (2,0) channels in I^{4+}

The delay-dependent kinetic energy release distribution for the channels leading to the formation of the I^{4+} ion is qualitatively different from that of all other observed iodine charge states. Channel III appears significantly broader for this ion, and there are two separate contributions of similar intensity to Channel II which can be resolved particularly for longer pump-probe delays. This is shown in Figure 7, which displays the ion image and corresponding KER distribution for the I^{4+} ion for pump-probe delays beyond 2 ps, where the Coulombic repulsion between the iodine and methyl sites following XUV absorption can be assumed to be minimal. For comparison, the image and KER distribution for the I^{5+} ion for the same pump-probe delay range is also displayed. It can be observed that the higher KER pump-probe channel (II) comprises two separate features in the I^{4+} ion, centered at KERs of approximately 5.5 and 9.5 eV. In contrast, only the lower energy of these two features is seen in the I^{5+} ion (or any other charge state). By comparison to the IR-only data, the first feature matches very well with the (1,1) Coulomb explosion by the IR alone, as expected. The higher energy feature observed in the I^{4+} ion matches very well in KER with the (1,2) observed in the IR-only data for the I^{2+} ion. This implies that IR-induced dissociations resulting in a I^{2+} ion are preferentially observed in the I^{4+} ion in the pump-probe experiment, whereas the pump-probe features observed in other highly charged ions predominantly originate from I^+ ions generated by the IR. As the IR produces significantly more I^+ than I^{2+} (in an approximately 3:1 ratio), this is to be expected, but it is therefore surprising that the (1,2) Coulomb explosion is observed so strongly in the I^{4+} ion in the pump-probe experiment. We believe this is due to the relative probabilities of different numbers of Auger decays following I(4d) photoabsorption by the iodine cation and dication.

The single-photon XUV photoionization dynamics of I^+ and I^{2+} has been studied previously by Kjeldsen *et al.*[80], who measured absolute photoionization cross-sections for different possible iodine final charge states. At the photon energy of the current work, 95 eV, the measured X-ray photoionization cross-section of I^+ to yield I^{3+} is approximately 50 times greater than the cross-section for I^{4+} production. Similarly, the cross-section for ionization of I^{2+} to I^{4+} is more than an order of magnitude greater than the cross-section for

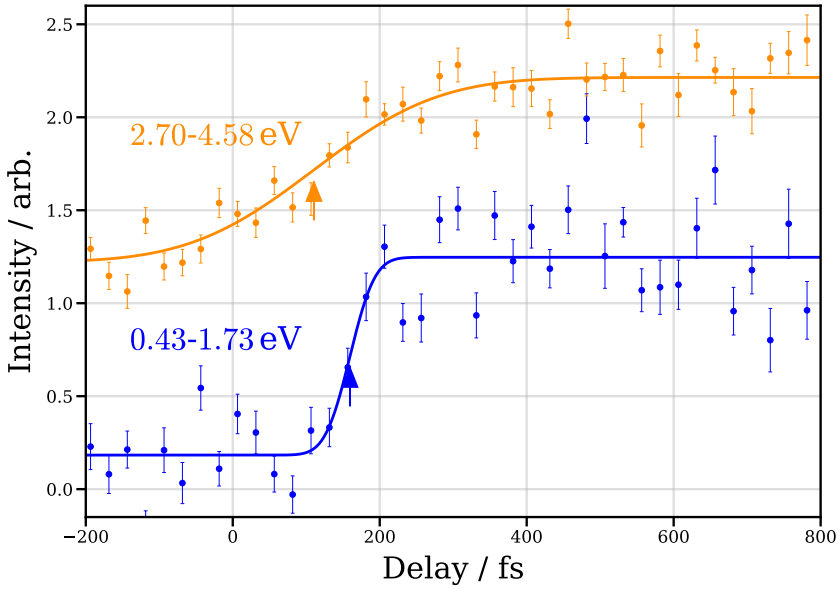

Fig. 8 Ion yields as a function of pump-probe delay for Channel I in the I^{4+} ion integrated over different ranges of kinetic energy release, as indicated. These have been fit to a Gaussian CDF as described in the text, and the centres of the CDF fits are marked with coloured arrows.

ionization of I^{2+} to I^{3+}. The domination of double ionization upon single photon absorption for the both the I^+ and I^{2+} ions provide a satisfactory explanation for why the I^{4+} ion selectively shows features arising from production of I^{2+} by the IR in the pump-probe experiment.

This propensity for IR-induced I^{2+} channels to be mapped to the I^{4+} ion is further seen in the time-dependence of the intensity of Channel III, as mentioned earlier. As seen in Figure 5, the intensity of low kinetic energy ($\sim$<5 eV KER) I^{4+} ions rises at considerably shorter pump-probe delays than expected. However, as shown in Figure 8, by further filtering on KER, it can be seen that the lowest KER I^{4+} ions (0.43-1.73 eV) rise in intensity at significantly later pump-probe delays than those of higher KER (2.70-4.58 eV). These two KER ranges were chosen to approximately overlap with contributions from the (0,1) and (0,2) channels, respectively. This dependence on KER is expected, as higher KER ions have a higher relative velocity, and so will reach greater internuclear separations more quickly, at which charge transfer no longer occurs. As shown in Figure 6, the onset times extracted from these KER-resolved fits match well with predictions by the classical OTB model.

4.3 Recoil-frame covariance imaging

In the previous discussion relating to the measured delay-dependent kinetic energies of given iodine charge states, the identity of the cofragment(s) originating from the same precursor methyl iodide molecule is unknown. As discussed in Section 4.3, recoil-frame covariance analysis can be used to extract relative velocity distributions for a given pair of ions. In this section, we demonstrate several examples in which such analysis can identify different channels which cannot be isolated through analysing the delay-dependent ion velocity distributions shown previously. As such, recoil-frame covariance analysis can be used in the present work to obtain a more complete picture of the multiple fragmentation, ionization and charge-transfer pathways possible.

Example recoil-frame covariance images for the I^{n+} (n=3-6) ion in covariance with the CH_x^+ ion for pump-probe delays greater than

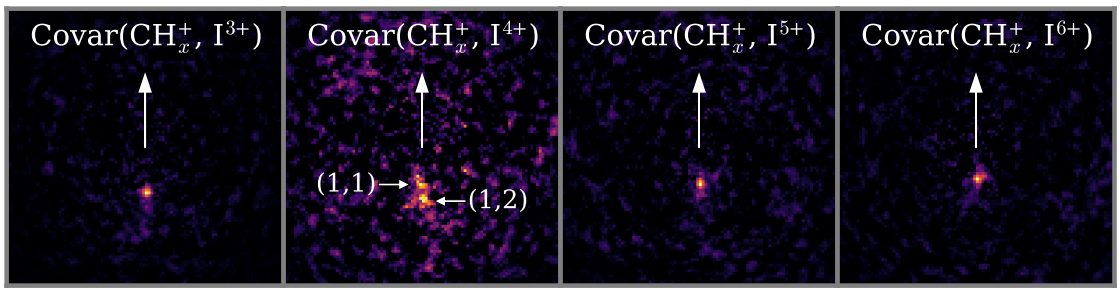

Fig. 9 Example recoil-frame covariance images for I^{n+} (n=3-6) with the CH_x^+ ion as a reference, integrated for pump-probe delays greater than 2 ps. The velocity of the reference ion is constricted to the vertical, as indicated by the white arrow.

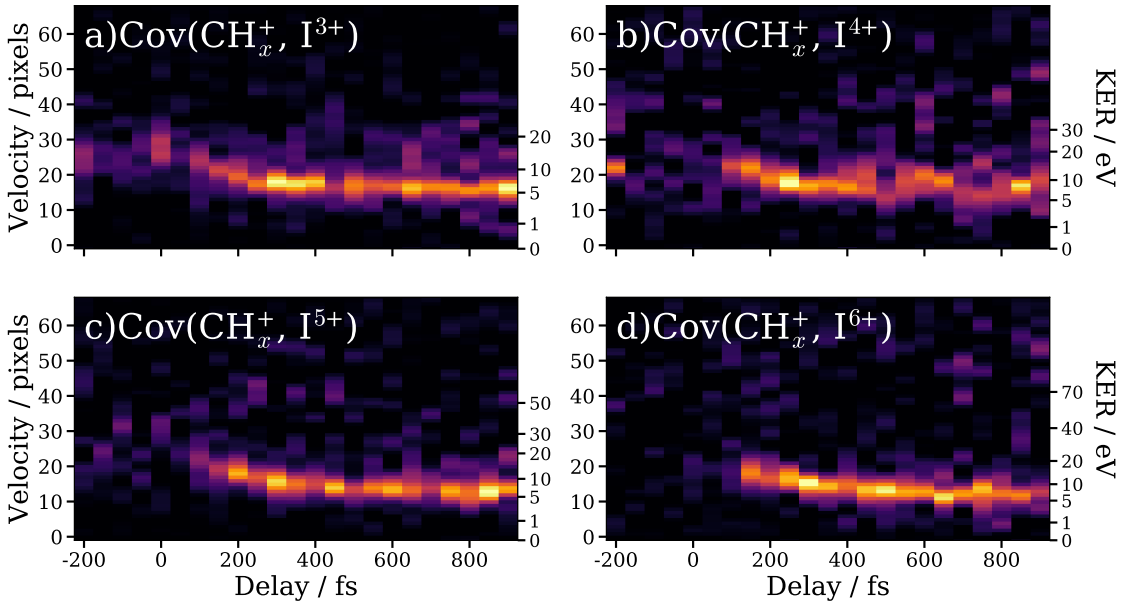

Fig. 10 Delay-dependent velocity distributions extracted from recoil-frame covariance maps between the CH_x^+ ions and I^{n+} ions.

2 ps are displayed in Figure 9. Although the exact number of hydrogens in the CH_x^+ cannot be resolved in the current data, a time-of-flight window is employed here for which the CH_3^+ is believed to be the dominant contribution. In all cases, clear signal at a recoil angle of 180 degrees is observed, as would be expected for a two-body fragmentation. Comparing the velocity distribution of these images with the non-covariance velocity distributions of the various iodine charge states confirms that the observed feature(s) correspond to Channel II. The low kinetic energy Channel III is not observed in covariance, as it arises from dissociations in which no charged methyl fragment is produced. The high kinetic energy Channel I originating from XUV-induced Coulomb explosion of intact CH_3I molecules is also not observed in Figure 9. This may be because the very high velocity methyl fragment associated with these Coulomb explosions from high charge states of CH_3I^+ leads to the CH_x^+ ions missing the detector for the majority of solid angles of the Newton sphere. The maximum velocity of CH_3I^+ ions which can be detected for all solid angles corresponds to a KER of approximately 20 eV. In the case of the I^{4+} ion, two channels can be clearly distinguished through the recoil-frame analysis, once more supporting their earlier assignments to (1,1) and (1,2) Coulomb explosions by the IR pulse. Both of these channels are associated with formation of CH_x^+ ions and should therefore be seen in covariance.

Through appropriate binning of the data, recoil-frame covariance maps can be calculated as a function of pump-probe delay, as demonstrated in Figure 10. Here, the data were grouped into 50 fs delay bins, resulting in ~5000-10000 laser shots per pump-probe delay. Despite the rather limited statistics, and the inherently unstable FEL, the resultant covariance images are of sufficient quality to extract delay-dependent correlated velocity distributions, as plotted in Figure 10 for selected ions in covariance with CH_3^+. The velocity distributions for each pump-probe delay are extracted by integrating the corresponding recoil-frame covariance images over a small angular range around 180 degrees to the vertical. The resulting distributions highlight the feature associated with a shifting KER as a function of delay (as described in detail in Section 4.2.2) - corroborating the assignment of this channel to (1,1) Coulomb explosion by the IR pulse followed by further ionization at the iodine site by the XUV pulse.

Thus far, discussion of the results presented has focused on channels in which the probe pulse ionizes at the iodine site-selectively. However, given the very high peak intensities at the focus of the XUV laser in the present work ($\sim 2\times10^{15}$ W/cm^2)), some level of ionization at the methyl fragment is likely. In principle, computing the covariance between I^{n+} and fragments other than CH_3^+ can isolate features involving additional photoionization at the methyl site (or alternatively, charge transfer between CH_3^+ and highly charged iodine ions). However, this is complicated by possible fragmentation of CH_3^{n+} ions by proton loss. Unfortunately, as mentioned previously, the mass resolution of the current experiment does not allow CH_3^+, CH_2^+, CH^+, C^+ to be discriminated. Nonetheless, it can be reasonably assumed that the earliest region in time-of-flight of the CH_x^+ peak arises predominantly from CH_x^+ ions with $x < 3$ (these ions are henceforth referred to as CH_y^+). Figure 11 displays delay-dependent covariance velocity distributions using ions in this time-of-flight region as the reference ions, with the aim of isolating channels associated with further ionization and fragmentation at the methyl site. The marked qualitative difference between these results and those presented in Figure 10 support the assumption that the two time-of-flight regions used correspond to different ion masses.

As shown in Figure 11, a feature with a delay-dependent kinetic energy release is seen only for iodine charge states greater than 4. For I^{5+} and I^{6+}, this feature closely resembles the analogous channel shown in Figure 10. These features can be seen to exist at long delays following the initial (1,1) Coulomb explosion, at which charge-transfer is prohibited. This strongly implies that this channel can

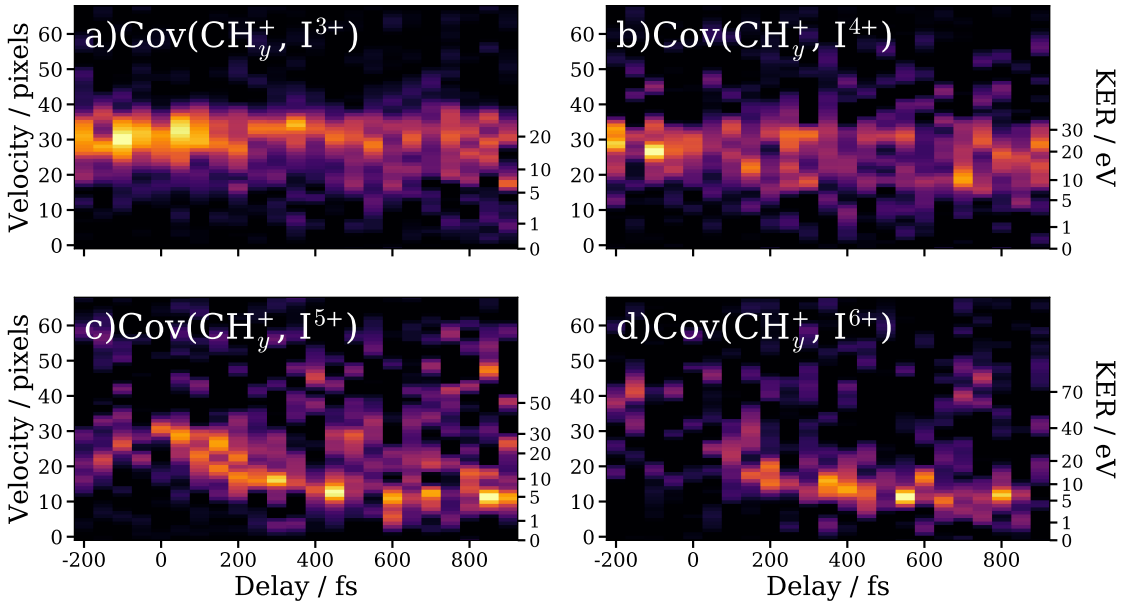

Fig. 11 Delay-dependent velocity distributions extracted from recoil-frame covariance maps between the CH_y^+ ions and I^{n+} ions with $y < 3$.

arise due to additional photoionization and subsequent fragmentation of dissociated CH_3^+ ions by the XUV. The observation that this feature is only observed for iodine charge states greater than 4 is then surprising, as the XUV photoabsorption cross-section for the methyl ion should not depend on the extent of XUV ionization of the I^+. The most reasonable explanation for this is an effect due to averaging over the small (10 μm) focal volume of the XUV laser. Higher iodine charge states most likely to be formed close to the focus, where, due to the higher peak laser intensity, the CH_3^+ ions are also more likely to absorb an XUV photon.

Upon multiple ionization of CH_3I by the XUV pulse, several Coulomb explosion pathways resulting in C^{2+} formation are possible. Evidence for explosions to yield C^{2+} (or even C^{3+}) can be seen in the yield of I^{n+} ions with kinetic energies significantly exceeding those predicted by Coulomb's Law assuming only a single charge at the methyl site (see Figure 4). Covariance between C^{2+} and I^{n+} ions can be calculated to probe such explosion pathways, and covariance velocity distributions for these ion pairs are plotted as a function of pump-probe delay in Figure 12. For all pump-probe delays, there is solely a high KER channel arising from Coulomb explosions to C^{2+} and I^{n+}. It should be noted that the in the plane of the detector, the maximum kinetic energy which can be detected for the C^{2+} ion is approximately twice that of the CH_3^+ ion, as expected given typical velocity-mapping ion optics[42]. For each iodine charge state, this feature depletes shortly after time-zero, as a result of dissociation of target molecules by the IR. This depletion does not occur at the same pump-probe delay for all the probed iodine charge states, and can be seen to systematically shift to later pump-probe delays for higher charges. This is highlighted by the fits of the integrated covariance signal as a function of pump-probe delay to Gaussian CDF functions, whose centres shift to later delays for higher charge states. While the precise origin of this behaviour is difficult to ascertain (due to the multiple possible fragmentation and ionization pathways involved), it is likely indicative of charge transfer channels which can occur shortly after dissociation by the IR pulse, and can occur over greater internuclear distances for higher iodine charge states.

5 Conclusions

In conclusion, we have presented results from a femtosecond multi-mass velocity-map ion imaging study into dynamics of methyl iodide following strong-field ionization and subsequent further ionization by an intense XUV pulse, predominantly at the iodine 4d orbital. Detailed analysis of the delay-dependent kinetic energy distributions of different iodine charge states provides a range of insights into the underlying ionization, dissociation and charge-transfer dynamics. Channels with a delay-dependent kinetic energy release as a result of a distance-dependent Coulomb repulsion were observed, and detailed analysis of these allows visualization of wavepacket motion on the CH_3I^{2+} potential energy surfaces populated by the pump pulse. As demonstrated previously[23], integrated yields of low kinetic energy ions are indicative of charge-transfer processes between recoiling highly charged iodine ions and neutral methyl fragments at short internuclear distances. Analysis of these transients extracted critical charge-transfer times for different charge states, which are consistent with a classical over-the-barrier model.

The integration of a fast timestamping camera with a conventional velocity-map imaging spectrometer provides the unique opportunity to extract correlated velocity distributions for individual ion pairs through recoil-frame covariance analysis[35,36,38]. Performing such analysis as a function of pump-probe delay yielded additional insight into a number of fragmentation/ionization channels possible in the present experiment. The ability to perform such analysis, despite limited experimental statistics and an inherently noisy free-electron laser is very promising for future experimental work, particularly given ongoing technical developments in high repetition rate

facilities, such as European XFEL and LCLS II. As shown here for the relatively simple CH_3I molecule, many fragmentation channels are populated and the ability to isolate individual dissociation pathways through covariance analysis is very valuable.

Conflicts of interest

There are no conflicts to declare.

Acknowledgements

The experiment was performed at SACLA with the approval of JASRI and the program review committee (proposal Nos. 2019B8054 Ueda and 2019B8063 Forbes). We thank the technical and scientific staff of SACLA for their hospitality and support before and during the beamtime. F.A. thanks the EPSRC and Magdalen College, Oxford for support. R.S.M. and J.W. thank the EPSRC for funding (EP/R010609/1). B.D.W. thanks the Central Laser Facility and Chemistry at the University of Southampton for a studentship. M.Bu. (EP/S028617/1), C.V. and M.Br. (EP/L005913/1) acknowledge support for EPSRC. We acknowledge support by the AMOS Program, Chemical Sciences, Geosciences, and Biosciences Division, Office of Basic Energy Sciences, Office of Science, US Department of Energy (R.F., J.O'N., N.W., T.D., and P.B.), Grants No. DE-SC0019451 (D.R., A.R.), and DE-FG02-86ER13491 (F.Z.). R.S.M., J.W. and B.D.W. gratefully acknowledge travel support from the UK Hub for the Physical Sciences on XFELS (STFC). H. F., K. N., and K. U acknowledge support by by the Xray Free Electron Laser Utilization Research Project and the X-ray Free Electron Laser Priority Strategy Program of the Ministry of Education, Culture, Sports, Science and Technology of Japan (MEXT), by the Japan Society for the Promotion of Science (JSPS) KAKENHI Grant No. 21244042, No. 23241033, No. 15K17487, No. 16K05016, by "Dynamic Alliance for Open Innovation Bridging Human, Environment and Materials" from the Ministry of Education, Culture, Sports, Science and Technology of Japan (MEXT) MEXT KAKENHI Grant No. 22740264, A.N. acknowledges support from the Research Program for Next Generation Young

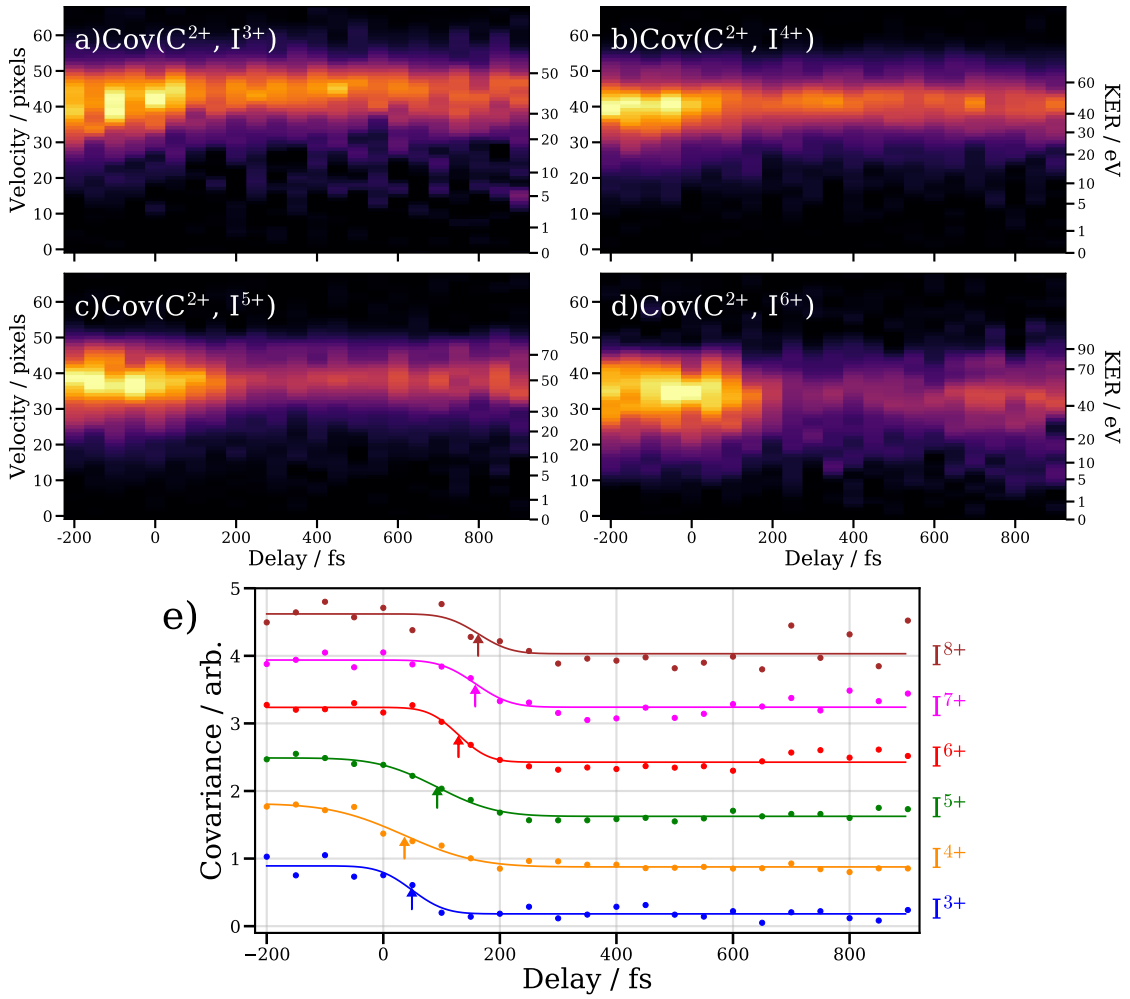

Fig. 12 Delay-dependent velocity distributions extracted from recoil-frame covariance maps between the C^{2+} ions and a) I^{3+}, b) I^{4+}, c) I^{5+} and d) I^{4+}. Panel e) displays the integrated covariance as a function of pump-probe delay for the C^{2+}, I^{n+} (n=3-8) ion pairs. These have been fit to a Gaussian CDF as described in the text, with the centres of the CDF fits marked by coloured arrows

Scientists of “Dynamic Alliance for Open Innovation Bridging Human, Environment and Materials” in “Network Joint Research Center for Materials and Devices”, and D.Y. acknowledges support by a Grant-in-Aid of Tohoku University Institute for Promoting Graduate Degree Programs Division for Interdisciplinary Advanced Research and Education.

Notes and references

1 V. May and Kühn, *Charge and Energy Transfer Dynamics in Molecular Systems*, John Wiley Sons, 2011.

2 R. A. Marcus, *Rev. Mod. Phys.*, 1993, **65**, 599–610.

3 H. J. Wörner, C. A. Arrell, N. Banerji, A. Cannizzo, M. Chergui, A. K. Das, P. Hamm, U. Keller, P. M. Kraus, E. Liberatore, P. Lopez-Tarifa, M. Lucchini, M. Meuwly, C. Milne, J.-E. Moser, U. Rothlisberger, G. Smolentsev, J. Teuscher, J. A. van Bokhoven and O. Wenger, *Structural Dynamics*, 2017, **4**, 061508.

4 R. Croce and H. van Amerongen, *Nat. Chem. Biol.*, 2014, **10**, 492–501.

5 T. Mirkovic, E. E. Ostroumov, J. M. Anna, G. Rienk van Grondelle and G. D. Scholes, *Chem. Rev.*, 2017, **117**, 249–293.

6 K. Dennerl, *Space. Sci. Rev.*, 2010, 57.

7 T. L. Thompson and J. T. Yates, *Topics in Catalysis*, 2005, **35**, 492–501.

8 L. Belshaw, F. Calegari, M. J. Duffy, A. Trabattoni, L. Poletto, M. Nisoli and J. B. Greenwood, *J. Phys. Chem. Lett.*, 2012, **3**, 3751–3754.

9 F. Calegari, D. Ayuso, A. Trabattoni, L. Belshaw, S. De Camillis, S. Anumula, F. Frassetto, L. Poletto, A. Palacios, P. Decleva, J. B. Greenwood, F. Martín and M. Nisoli, *Science*, 2014, **346**, 336–339.

10 A. Ludwig, E. Liberatore, J. Herrmann, L. Kasmi, P. López-Tarifa, L. Gallmann, U. Rothlisberger, U. Keller and M. Lucchini, *J. Phys. Chem. Lett.*, 2016, **7**, 1901–1906.

11 K. S. Schanze and K. Sauer, *J. Am. Chem. Soc.*, 1988, **110**, 1180–1186.

12 M. Maus, W. Rettig, D. Bonafoux and R. Lapouyade, *J. Phys. Chem. A*, 1999, **103**, 3388–3401.

13 M. Ferray, A. LHuillier, X. F. Li, L. A. Lompre, G. Mainfray and C. Manus, 1988, **21**, 31–35.

14 W. Ackermann, G. Asova, V. Ayvazyan *et al.*, *Nat. Photonics*, 2007, **1**, 336–342.

15 P. Emma, R. Akre and J. t. Arthur, *Nat. Photonics*, 2010, **4**, 641–647.

16 T. Ishikawa, H. Aoyagi and T. t. Asaka, *Nat. Photonics*, 2012, **6**, 540–544.

17 B. Erk, D. Rolles, L. Foucar, B. Rudek, S. W. Epp, M. Cryle, C. Bostedt, S. Schorb, J. Bozek, A. Rouzee, A. Hundertmark, T. Marchenko, M. Simon, F. Filsinger, L. Christensen, S. De, S. Trippel, J. Küpper, H. Stapelfeldt, S. Wada, K. Ueda, M. Swiggers, M. Messerschmidt, C. D. Schröter, R. Moshammer, I. Schlichting, J. Ullrich and A. Rudenko, *Phys. Rev. Lett.*, 2013, **110**, 053003.

18 K. Motomura, E. Kukk, H. Fukuzawa and *et al.*, *J. Chem. Phys. Lett.*, 2015, **6**, 2944–2949.

19 K. Nagaya, K. Motomura, E. Kukk, H. Fukuzawa, S. Wada, T. Tachibana, Y. Ito, S. Mondal, T. Sakai, K. Matsunami, R. Koga, S. Ohmura, Y. Takahashi, M. Kanno, A. Rudenko, C. Nicolas, X.-J. Liu, Y. Zhang, J. Chen, M. Anand, Y. H. Jiang, D.-E. Kim, K. Tono, M. Yabashi, H. Kono, C. Miron, M. Yao and K. Ueda, *Phys. Rev. X*, 2016, **6**, 021035.

20 A. Rudenko, L. Inhester, K. Hanasaki, X. Li, S. J. Robatjazi, B. Erk, R. Boll, K. Toyota, Y. Hao, C. Vendrell, O. Bomme, E. Savelyev, B. Rudek, L. Foucar, S. H. Southworth, C. S. Lehmann, B. Kraessig, T. Marchenko, N. Simon, K. Ueda, K. R. Ferguson, M. Bucher, T. Gorkhover, S. Carron, R. Alonoso-Mori, J. E. Koglin, J. Correa, G. J. Williams, S. Boutet, L. Young, C. Bostedt, S. K. Son, R. Santra and D. Rolles, *Nature*, 2017, **546**, 129–132.

21 K. Schnorr, A. Senftleben, M. Kurka, A. Rudenko, G. Schmid, T. Pfeifer, K. Meyer, M. Kübel, M. F. Kling, Y. H. Jiang, R. Treusch, S. Düsterer, B. Siemer, M. Wöstmann, H. Zacharias, R. Mitzner, T. J. M. Zouros, J. Ullrich, C. D. Schröter and R. Moshammer, *Phys. Rev. Lett.*, 2014, **113**, 073001.

22 A. Picón, C. S. Lehmann and C. t. Bostedt, *Nat. Commun.*, 2016, **7**, 11652.

23 B. Erk, R. Boll, S. Trippel, D. Anielski, L. Foucar, B. Rudek, S. W. Epp, R. Coffee, S. Carron, S. Schorb, K. R. Ferguson, M. Swiggers, J. D. Bozek, M. Simon, T. Marchenko, J. Kupper, I. Schlichting, J. Ullrich, C. Bostedt, D. Rolles and A. Rudenko, *Science (80-.).*, 2014, **345**, 288–291.

24 R. Boll, B. Erk, R. Coffee, S. Trippel, T. Kierspel, C. Bomme, J. D. Bozek, M. Burkett, S. Carron, K. R. Ferguson, L. Foucar, J. Küpper, T. Marchenko, C. Miron, M. Patanen, T. Osipov, S. Schorb, M. Simon, M. Swiggers, S. Techert, K. Ueda, C. Bostedt, D. Rolles and A. Rudenko, *Struct. Dyn.*, 2016, **3**, 043207.

25 K. Amini, E. Savelyev, F. Braußе, N. Berrah, C. Bomme, M. Brouard, M. Burt, L. Christensen, S. Düsterer, B. Erk, H. Höppner, T. Kierspel, F. Krecinic, A. Lauer, J. W. L. Lee, M. Müller, E. Müller, T. Mullins, H. Redlin, N. Schirmel, J. Thøgersen, S. Techert, S. Toleikis, R. Treusch, S. Trippel, A. Ulmer, C. Vallance, J. Wiese, P. Johnsson, J. Küpper, A. Rudenko, A. Rouzée, H. Stapelfeldt, D. Rolles and R. Boll, *Struct. Dyn.*, 2018, **5**, 014301.

26 R. Forbes, F. Allum, S. Bari, R. Boll, M. Brouard, P. Bucksbaum, N. Ekanayake, B. Erk, A. Howard, P. Johnsson, J. Lee, B. Manschwetus, R. Mason, C. Passow, J. Peschel, D. Rivas, A. Roerig, A. Rouzee, C. Vallance, F. Ziaee, D. Rolles and M. Burt, *J. Phys. B*, 2020.

27 S. Owada, K. Togawa, T. Inagaki, T. Hara, T. Tanaka, Y. Joti, T. Koyama, K. Nakajima, H. Ohashi, Y. Senba, T. Togashi, K. Tono,

M. Yamaga, H. Yumoto, M. Yabashi, H. Tanaka and T. Ishikawa, *Journal of Synchrotron Radiation*, 2018, **25**, 282–288.
28 T. N. Olney, G. Cooper and C. Brion, *Chem. Phys.*, 1998, **232**, 211 – 237.
29 R. Forbes, A. De Fanis, C. Bomme, D. Rolles, S. T. Pratt, I. Powis, N. A. Besley, M. Simon, S. Nandi, A. R. Milosavljević, C. Nicolas, J. D. Bozek, J. G. Underwood and D. M. P. Holland, *J. Chem. Phys.*, 2018, **149**, 144302.
30 R. Forbes, A. De Fanis, C. Bomme, D. Rolles, S. T. Pratt, I. Powis, N. A. Besley, S. Nandi, A. R. Milosavljević, C. Nicolas, J. D. Bozek, J. G. Underwood and D. M. P. Holland, *J. Chem. Phys.*, 2018, **149**, 094304.
31 R. Forbes, A. D. Fanis, D. Rolles, S. T. Pratt, I. Powis, N. A. Besley, A. Milosavljevic, C. Nicolas, J. D. Bozek and D. M. P. Holland, *J. Phys. B*, 2020, **53**, 155101.
32 N. Saito and I. H. Suzuki, *Int. J. Mass Spectrom.*, 1992, **115**, 157 – 172.
33 A. Nomerotski, S. Adigun-Boaye, M. Brouard, E. Campbell, A. Clark, J. Crooks, J. John, A. Johnsen, C. Slater, R. Turchetta, C. Vallance, E. Wilman and W. Yuen, *Nucl. Instrum. Meth. A*, 2011, **633**, S243 – S246.
34 J. J. John, M. Brouard, A. Clark, J. Crooks, E. Halford, L. Hill, J. W. L. Lee, A. Nomerotski, R. Pisarczyk, I. Sedgwick, C. S. Slater, R. Turchetta, C. Vallance, E. Wilman, B. Winter and W. H. Yuen, *J. Instrum.*, 2012, **7**, C08001–C08001.
35 L. J. Frasinski, K. Codling and P. A. Hatherly, *Science (80-.).*, 1989, **246**, 1029–1031.
36 C. S. Slater, S. Blake, M. Brouard, A. Lauer, C. Vallance, J. J. John, R. Turchetta, A. Nomerotski, L. Christensen, J. H. Nielsen, M. P. Johansson and H. Stapelfeldt, *Phys. Rev. A*, 2014, **89**, 011401.
37 L. Christensen, J. H. Nielsen, C. B. Brandt, C. B. Madsen, L. B. Madsen, C. S. Slater, A. Lauer, M. Brouard, M. P. Johansson, B. Shepperson and H. Stapelfeldt, *Phys. Rev. Lett.*, 2014, **113**, 073005.
38 C. S. Slater, S. Blake, M. Brouard, A. Lauer, C. Vallance, C. S. Bohun, L. Christensen, J. H. Nielsen, M. P. Johansson and H. Stapelfeldt, *Phys. Rev. A*, 2015, **91**, 053424.
39 F. Allum, M. Burt, K. Amini, R. Boll, H. Köckert, P. K. Olshin, S. Bari, C. Bomme, F. Braußе, B. Cunha de Miranda, S. Düsterer, B. Erk, M. Géléoc, R. Geneaux, A. S. Gentleman, G. Goldsztejn, R. Guillemin, D. M. P. Holland, I. Ismail, P. Johnsson, L. Journel, J. Küpper, J. Lahl, J. W. L. Lee, S. Maclot, S. R. Mackenzie, B. Manschwetus, A. S. Mereshchenko, R. Mason, J. Palaudoux, M. N. Piancastelli, F. Penent, D. Rompotis, A. Rouzée, T. Ruchon, A. Rudenko, E. Savelyev, M. Simon, N. Schirmel, H. Stapelfeldt, S. Techert, O. Travnikova, S. Trippel, J. G. Underwood, C. Vallance, J. Wiese, F. Ziaee, M. Brouard, T. Marchenko and D. Rolles, *J. Chem. Phys.*, 2018, **149**, 204313.
40 S. Owada, M. Fushitani, A. Matsuda, H. Fujise, Y. Sasaki, Y. Hikosaka, A. Hishikawa and M. Yabashi, *Journal of Synchrotron Radiation*, 2020, **27**, 1362–1365.
41 H. Fukuzawa, K. Nagaya and K. Ueda, *Nuclear Instruments and Methods in Physics Research Section A: Accelerators, Spectrometers, Detectors and Associated Equipment*, 2018, **907**, 116 – 131.
42 A. T. J. B. Eppink and D. H. Parker, *Review of Scientific Instruments*, 1997, **68**, 3477–3484.
43 D. Rolles, R. Boll, B. Erk, D. Rompotis and B. Manschwetus, *J. Vis. Exp.*, 2018, e57055.
44 M. Krikunova, T. Maltezopoulos, A. Azima, M. Schlie, U. Frühling, H. Redlin, R. Kalms, S. Cunovic, N. M. Kabachnik, M. Wieland and M. Drescher, *New J. Phys.*, 2009, **11**, year.
45 M. Uiberacker, T. Uphues, M. Schultze, A. J. Verhoef, V. Yakovlev, M. F. Kling, J. Rauschenberger, N. M. Kabachnik, H. Schröder, M. Lezius, K. L. Kompa, H. G. Muller, M. J. Vrakking, S. Hendel, U. Kleineberg, U. Heinzmann, M. Drescher and F. Krausz, *Nature*, 2007, **446**, 627–632.
46 S. Owada, K. Nakajima, T. Togashi, T. Katayama, H. Yumoto, H. Ohashi and M. Yabashi, *Journal of Synchrotron Radiation*, 2019, **26**, 887–890.
47 G. A. Garcia, L. Nahon and I. Powis, *Rev. Sci. Instrum.*, 2004, **75**, 4989–4996.
48 M. E. Corrales, G. Gitzinger, J. González-Vázquez, V. Loriot, R. de Nalda and L. Bañares, *J. Phys. Chem. A*, 2012, **116**, 2669–2677.
49 L. J. Frasinski, *J. Phys. B*, 2016, **49**, 152004.
50 L. J. Frasinski, V. Zhaunerchyk, M. Mucke, R. J. Squibb, M. Siano, J. H. Eland, P. Linusson, P. V.d. Meulen, P. Salén, R. D. Thomas, M. Larsson, L. Foucar, J. Ullrich, K. Motomura, S. Mondal, K. Ueda, T. Osipov, L. Fang, B. F. Murphy, N. Berrah, C. Bostedt, J. D. Bozek, S. Schorb, M. Messerschmidt, J. M. Glownia, J. P. Cryan, R. N. Coffee, O. Takahashi, S. Wada, M. N. Piancastelli, R. Richter, K. C. Prince and R. Feifel, *Phys. Rev. Lett.*, 2013, **111**, 073002.
51 O. Kornilov, M. Eckstein, M. Rosenblatt, C. P. Schulz, K. Motomura, A. Rouzée, J. Klei, L. Foucar, M. Siano, A. Lübcke, F. Schapper, P. Johnsson, D. M. Holland, T. Schlathölter, T. Marchenko, S. Düsterer, K. Ueda, M. J. Vrakking and L. J. Frasinski, *J. Phys. B At. Mol. Opt. Phys.*, 2013, **46**, 164028.
52 M. Mucke, V. Zhaunerchyk, L. J. Frasinski, R. J. Squibb, M. Siano, J. H. D. Eland, P. Linusson, P. Salén, P. v. d. Meulen, R. D. Thomas, M. Larsson, L. Foucar, J. Ullrich, K. Motomura, S. Mondal, K. Ueda, T. Osipov, L. Fang, B. F. Murphy, N. Berrah, C. Bostedt, J. D. Bozek, S. Schorb, M. Messerschmidt, J. M. Glownia, J. P. Cryan, R. N. Coffee, O. Takahashi, S. Wada, M. N. Piancastelli, R. Richter, K. C. Prince and R. Feifel, *New J. Phys.*, 2015, **17**, 073002.

53 D. You, H. Fukuzawa, Y. Luo, S. Saito, M. Berholts, T. Gaumnitz, M. Huttula, P. Johnsson, N. Kishimoto, H. Myllynen, A. Nemer, A. Niozu, M. Patanen, E. Pelimanni, T. Takanashi, S. I. Wada, N. Yokono, S. Owada, K. Tono, M. Yabashi, K. Nagaya, E. Kukk and K. Ueda, *Phys. Chem. Chem. Phys.*, 2020, **22**, 2648–2659.

54 J. W. L. Lee, H. Köckert, D. Heathcote, D. Popat, R. T. Chapman, G. Karras, P. Majchrzak, E. Springate and C. Vallance, *Commun. Chem.*, 2020, **3**, 72.

55 M. Burt, K. Amini, J. W. Lee, L. Christiansen, R. R. Johansen, Y. Kobayashi, J. D. Pickering, C. Vallance, M. Brouard and H. Stapelfeldt, *J. Chem. Phys.*, 2018, **148**, 091102.

56 J. D. Pickering, K. Amini, M. Brouard, M. Burt, I. J. Bush, L. Christensen, A. Lauer, J. H. Nielsen, C. S. Slater and H. Stapelfeldt, *J. Chem. Phys.*, 2016, **144**, 161105–161105.

57 P. Graham, K. W. Ledingham, R. P. Singhai, S. M. Hankin, T. McCanny, X. Fang, C. Kosmidis, P. Tzallas, P. F. Taday and A. J. Langley, *J. Phys. B At. Mol. Opt. Phys.*, 2001, **34**, 4015–4026.

58 H. Liu, Z. Yang, Z. Gao and Z. Tang, *J. Chem. Phys.*, 2007, **126**, 044316.

59 Y. Wang, S. Zhang, Z. Wei and B. Zhang, *J. Phys. Chem. A*, 2008, **112**, 3846–3851.

60 S. G. Walt, N. Bhargava Ram, A. Von Conta, O. I. Tolstikhin, L. B. Madsen, F. Jensen and H. J. Wörner, *J. Phys. Chem. A*, 2015, **119**, 11772–11782.

61 D. Zhang, S. Luo, H. Xu, M. Jin, F. Liu, B. Yan, Z. Wang, H. Liu, D. Jiang, A. Eppink, W. Roeterdink, S. Stolte and D. Ding, *Eur. Phys. J. D*, 2017, **71**, 148.

62 Z. Wei, J. Li, S. T. See and Z. H. Loh, *J. Phys. Chem. Lett.*, 2017, **8**, 6067–6072.

63 Y. Malakar, W. L. Pearson, M. Zohrabi, B. Kaderiya, P. Kanaka Raju, F. Ziaee, S. Xue, A. T. Le, I. Ben-Itzhak, D. Rolles and A. Rudenko, *Phys. Chem. Chem. Phys.*, 2019, **21**, 14090–14102.

64 M. E. Corrales, J. González-Vázquez, R. De Nalda and L. Banares, *J. Phys. Chem. Lett.*, 2019, **10**, 138–143.

65 G. N. Gibson, M. Li, C. Guo and J. P. Nibarger, *Phys. Rev. A - At. Mol. Opt. Phys.*, 1998, **58**, 4723–4727.

66 C. Guo, M. Li and G. N. Gibson, *Phys. Rev. Lett.*, 1999, **82**, 2492–2495.

67 C. Guo, M. Li, J. P. Nibarger and G. N. Gibson, *Phys. Rev. A - At. Mol. Opt. Phys.*, 2000, **61**, 6.

68 J. P. Nibarger, S. V. Menon and G. N. Gibson, *Phys. Rev. A - At. Mol. Opt. Phys.*, 2001, **63**, 12.

69 S. V. Menon, J. P. Nibarger and G. N. Gibson, *J. Phys. B At. Mol. Opt. Phys.*, 2002, **35**, 2961–2974.

70 W. Lai and C. Guo, *Phys. Rev. A*, 2015, **92**, 013402.

71 W. Lai and C. Guo, *J. Phys. B At. Mol. Opt. Phys.*, 2016, **49**, 225601.

72 H. Stapelfeldt, E. Constant and P. B. Corkum, *Phys. Rev. Lett.*, 1995, **74**, 3780–3783.

73 M. Burt, R. Boll, J. W. Lee, K. Amini, H. Köckert, C. Vallance, A. S. Gentleman, S. R. Mackenzie, S. Bari, C. Bomme, S. Düsterer, B. Erk, B. Manschwetus, E. Müller, D. Rompotis, E. Savelyev, N. Schirmel, S. Techert, R. Treusch, J. Küpper, S. Trippel, J. Wiese, H. Stapelfeldt, B. C. De Miranda, R. Guillemin, I. Ismail, L. Journel, T. Marchenko, J. Palaudoux, F. Penent, M. N. Piancastelli, M. Simon, O. Travnikova, F. Brausse, G. Goldsztejn, A. Rouzée, M. Géléoc, R. Geneaux, T. Ruchon, J. Underwood, D. M. Holland, A. S. Mereshchenko, P. K. Olshin, P. Johnsson, S. Maclot, J. Lahl, A. Rudenko, F. Ziaee, M. Brouard and D. Rolles, *Phys. Rev. A*, 2017, **96**, 043415.

74 X. Ding, R. Forbes, M. Kübel, K. F. Lee, M. Spanner, A. Y. Naumov, D. M. Villeneuve, A. Stolow, P. B. Corkum and A. Staudte, *J. Chem. Phys.*, 2019, **151**, 174301.

75 H. Ryufuku, K. Sasaki and T. Watanabe, *Phys. Rev. A*, 1980, **21**, 745–750.

76 E. Hamilton, T. Seideman, T. Ejdrup, M. D. Poulsen, C. Z. Bisgaard, S. S. Viftrup and H. Stapelfeldt, *Phys. Rev. A - At. Mol. Opt. Phys.*, 2005, **72**, 043402.

77 L. Verlet, *Phys. Rev.*, 1967, **159**, 98–103.

78 A. Niehaus, *J. Phys. B*, 1986, **19**, 2925–2937.

79 S. M. Poullain, D. V. Chicharro, J. Gonzá Lez-Vá, L. Rubio-Lago and L. Bañ Ares, *Phys. Chem. Chem. Phys. Phys. Chem. Chem. Phys*, 2017, **7886**, 7886–7896.

80 H. Kjeldsen, P. Andersen, F. Folkmann, H. Knudsen, B. Kristensen, J. B. West and T. Andersen, *Phys. Rev. A - At. Mol. Opt. Phys.*, 2000, **62**, 020702–020701.